Eur. Phys. J. B **29**, 553–559 (2002)
DOI: 10.1140/epjb/e2002-00339-x

THE EUROPEAN
PHYSICAL JOURNAL B

Balance-equation approach to impact ionization induced by an intense terahertz radiation: Application to InAs/AlSb heterojunctions

J.C. Cao[1,a] and X.L. Lei[2]

[1] State Key Laboratory of Functional Materials for Informatics, Shanghai Institute of Microsystem and Information Technology, Chinese Academy of Sciences, 865 Changning Road, Shanghai 200050, PR China
[2] Department of Physics, Shanghai Jiaotong University, 1954 Huashan Road, Shanghai, 200030, PR China, and State Key Laboratory of Functional Materials for Informatics, Shanghai Institute of Microsystem and Information Technology, Chinese Academy of Sciences, 865 Changning Road, Shanghai 200050, PR China

Received 24 May 2002 / Received in final form 26 August 2002
Published online 31 October 2002 – © EDP Sciences, Società Italiana di Fisica, Springer-Verlag 2002

Abstract. We have extended the balance equations to account for conduction-valence interband impact ionization (II) process induced by an intense terahertz (THz) electromagnetic irradiation in semiconductors, and applied them to study the II effect on electron transport and electron-hole pair generation-recombination rate in THz-driven InAs/AlSb heterojunctions (HJ). As many as needed multiphoton channels are self-consistently taken into account for yielding a given accuracy. The time evolution of transport state including THz-radiation-induced II process are monitored in details by an extensive time-dependent analysis. Two different physical stages, the quasi-steady state and the complete steady-state, are clearly identified from the present calculations. Intersubband electron transfer rate and net electron-hole generation rate are derived as functions of the THz radiation strength $E_{\rm ac}$ for various radiation frequencies from $f_{\rm ac} = 0.42$ to 6 THz at lattice temperatures $T = 6$ K. It's indicated that the THz radiation with a larger $E_{\rm ac}$ or a lower $f_{\rm ac}$, has a stronger effect on electron transport and II process. Qualitative agreement is obtained between the calculated electron-hole generation rate and the available experimental data for InAs/AlSb HJ's at $T = 6$ K.

PACS. 73.50.Fq High-field and nonlinear effects – 72.10.-d Theory of electronic transport; scattering mechanisms – 72.20.-i Conductivity phenomena in semiconductors and insulators

1 Introduction

Due to the development of the terahertz (THz) free-electron laser, nonlinear dynamics involving electron transport in low-dimensional semiconductors driven by an intense THz electromagnetic radiation has become a central focus of many experimental and theoretical studies [1–12]. Under the influence of THz radiation, low-dimensional electron gas exhibits many interesting phenomena, such as THz-radiation-induced dc current suppression [1], multiphoton-assisted resonant tunneling [2], negative absolute resistance [3], and Shapiro steps on dc current-voltage curve [4]. Recently, Markelz *et al.* [5] used far-infrared transmissions, reflections, and dc photoconductivity measurements to study impact ionization caused by THz radiations in InAs/AlSb heterojunctions (HJ), and demonstrated that the carrier multiplication occurs in InAs/AlSb HJ's driven by THz fields. These experimental advances motivated new theoretical interests in THz optic-electronics [6–12]. One of the authors recently developed a new balance-equation approach [6–8] to electron transport in semiconductors driven by an intense THz radiation field. In this set of momentum and energy balance equations [6–8] the slowly varying part of the center-of-mass is distinguished from the rapid oscillating part of it, and all the multiphoton process due to the intense THz radiation are included. This set of equations, which allow one to investigate experimentally measured quantities during a THz-driven transport without following the rapidly-oscillating time-dependent driving field, has been successfully used to study the effect of an intense THz radiation on electron transport in quasi-two-dimensional systems [6,7] and in superlattice minibands [8]. Study of THz–radiation-induced II process is, however, still lacking up to now.

[a] e-mail: jccao8@hotmail.com

Impact ionization and Auger recombination processes, as basic mechanisms for carrier generation and recombination, can affect properties of devices essentially. The theory describing the processes, therefore, becomes an important subject for both semiconductor physics and device applications. The recent development of InAs-based devices [15–18], such as infrared electro-optic modulators [15], far-infrared optical mixers [16], giant third harmonic generations [17], and interband cascade light emitting diodes [18], requires an understanding of high-field electron transport and II process at the operation frequencies in the THz range.

The purpose of this work is to extend the balance equation approach [6–8] to include II process [19,20] induced by an intense THz radiation in two-dimensional (2D) semiconductor systems, and apply them to study the II effect on electron transport and electron-hole generation rate in InAs/AlSb HJ's driven by THz radiations having various frequency and strength. In the present approach, II and Auger process are treated as a kind of scattering mechanisms. Time-dependent electron velocity, electron temperature, electron-hole generation rate, and the order of multiple photon channel are calculated by directly solving the set of balance equations. We present in some details the dependence of transport characteristics on THz radiation fields with and without accounting for the II process, and compare the calculated electron-hole generation rates with the available experiments [5] for InAs/AlSb 2D HJ at lattice temperature $T = 6$ K.

The remainders of the article are organized as follows. In Section 2 we present the acceleration-, energy-, and carrier-number-balance equations including II process under the influence of a uniform dc field and a THz electric field. In Section 3, these equations are applied to investigate transport characteristics, such as electron drift velocity, electron temperature, intersubband electron transfer, and multiple photon process in InAs/AlSb HJ's driven by THz radiations having different strength and frequency in the range of $0.42 \sim 6$ THz at $T = 6$ K. Finally, in Section 4 we draw the main conclusions.

2 Balance equations including II process driven by an intense THz radiation

We consider a semiconductor HJ with a 2D energy-wavevector relation $\varepsilon_s(\mathbf{k}_\parallel)$, where s is the subband index and $\mathbf{k}_\parallel = (k_x, k_y)$ is the 2D wave vector. When a uniform dc (or slowly varying) electric field $\mathbf{E}_0$ and a uniform sinusoidal radiation field with the frequency $f_{\rm ac}$ and the amplitude $E_{\rm ac}$,

$$\mathbf{E}(t) = \mathbf{E}_0 + \mathbf{E}_{\rm ac}\sin(2\pi f_{\rm ac} t), \tag{1}$$

are applied in the direction parallel to HJ interface, the transport quantities will undergo both the rapid oscillation (due to high-frequency radiation field) and the slow variation (due to E_0 and intrinsic relaxation times of the system). If we measure all the quantities as the average over a time interval much longer than the period of the radiation field, the carrier conduction can be described by the following equations for the force, the energy, and the carrier number balance [6–8,19,20] ($\hbar = 1 = k_{\rm B}$ throughout the paper)

$$\frac{\mathrm{d}\mathbf{v}}{\mathrm{d}t} = e\mathbf{E}_0 \cdot \mathcal{K} + \mathbf{A}_{\rm ei} + \mathbf{A}_{\rm ep} + \mathbf{A}_{\rm II} - g\mathbf{v}, \tag{2}$$

$$\frac{\mathrm{d}h_e}{\mathrm{d}t} = e\mathbf{E}_0 \cdot \mathbf{v} - W_{\rm ep} - W_{\rm II} - gh_e + S_{\rm p} + S_{\rm II}, \tag{3}$$

$$\frac{\mathrm{d}N}{\mathrm{d}t} = gN. \tag{4}$$

The above equations are the extension of the recently-developed balance equations [6–8] to include II process [19,20] in semiconductors driven by a THz electric field. The transport state of electrons is described by the effective momentum shift $\mathbf{p}_d$, electron temperature T_e, and electron chemical potential μ determined by electron sheet density

$$N = 2\sum_{s,\mathbf{k}_\parallel} f\left[\left(\varepsilon_s(\mathbf{k}_\parallel) - \mu\right)/T_e\right], \tag{5}$$

with $f(x) = 1/\left[\exp(x) + 1\right]$ the Fermi distribution function. On the other hand, since the effective hole mass is usually much larger than that of the electron, the drift movement and heating of hole gas are negligible in comparison with those of the electron gas, thus the hole gas can be described by the lattice temperature T and hole chemical potential μ^h. In equations (2–4), e is the carrier charge, g is the net electron-hole generation rate by balancing impact ionization generation and Auger recombination. The average velocity $\mathbf{v}$, average energy h_e, and the ensemble-averaged inverse effective mass tensor $\mathcal{K}$ of electrons are defined respectively by $\mathbf{v} = \left\langle \nabla\varepsilon_s\left(\mathbf{k}_\parallel\right)\right\rangle$, $h_e = \left\langle \varepsilon_s\left(\mathbf{k}_\parallel\right)\right\rangle$, and $\mathcal{K} = \left\langle \nabla\nabla\varepsilon_s\left(\mathbf{k}_\parallel\right)\right\rangle$, in which $\langle\cdots\rangle$ stands for the weighted integral: $\langle\cdots\rangle = 1/\left(2\pi^2 N\right)\sum_s \int\int \mathrm{d}k_x \mathrm{d}k_y f\left(\left(\bar{\varepsilon}_s\left(\mathbf{k}_\parallel\right) - \mu\right)/T_e\right)\ldots$, with $\bar{\varepsilon}_s\left(\mathbf{k}_\parallel\right) \equiv \varepsilon_s\left(\mathbf{k}_\parallel - \mathbf{p}_d\right)$. $\mathbf{A}_{\rm ei}$, $\mathbf{A}_{\rm ep}$, and $\mathbf{A}_{\rm II}$ are the frictional accelerations respectively due to electron-impurity scattering, electron-phonon scattering, and conduction-valence interband II process. $W_{\rm ep}$ and $W_{\rm II}$ are the energy-loss rates respectively due to electron-phonon scattering and conduction-valence interband II process. $S_{\rm p}$ and $S_{\rm II}$ are the energy-gain rates of the electron system from the radiation field through the multiphoton process ($n = \pm1, \pm2, ...$) in association with electron-phonon interaction and II process, respectively. For the parabolic energy band $\varepsilon_s(\mathbf{k}_\parallel) = \varepsilon_s + \mathbf{k}_\parallel^2/(2m)$ with ε_s the energy of the bottom of sth subband and m the effective electron mass, the expressions of $\mathbf{A}_{\rm ei}$, $\mathbf{A}_{\rm ep}$, and $W_{\rm ei}$ are found in reference [21]. The electron-hole generation rate g, II-induced

acceleration $A_{\rm II}$, and II-induced energy-loss rate $W_{\rm II}$ are respectively expressed by

$$g = \frac{2}{N}\sum_{s',s,\mathbf{k}_\|,\mathbf{q}_\|}\left|\widetilde{M}^{\rm II}_{s',s}\left(\mathbf{q}_\|\right)\right|^2 I(s',s,\mathbf{k}_\|,\mathbf{q}_\|), \qquad (6)$$

$$A_{\rm II} = \frac{2}{N}\sum_{s',s,\mathbf{k}_\|,\mathbf{q}_\|}\left|\widetilde{M}^{\rm II}_{s',s}\left(\mathbf{q}_\|\right)\right|^2 \frac{k_x}{m} I(s',s,\mathbf{k}_\|,\mathbf{q}_\|), \qquad (7)$$

$$W_{\rm II} = \frac{2}{N}\sum_{s',s,\mathbf{k}_\|,\mathbf{q}_\|}\left|\widetilde{M}^{\rm II}_{s',s}\left(\mathbf{q}_\|\right)\right|^2 \varepsilon^h_{\mathbf{k}_\|} I(s',s,\mathbf{k}_\|,\mathbf{q}_\|), \qquad (8)$$

with

$$I(s',s,\mathbf{k}_\|,\mathbf{q}_\|) = \sum_{n=-\infty}^{\infty} J_n^2(\mathbf{q}_\|\cdot\mathbf{r}_\omega)\Pi_2(s',s,\mathbf{q}_\|,\omega_2-n\omega) \times\left[f\left(\frac{\xi_{\mathbf{k}_\|-\mathbf{q}_\|}}{T_e}\right)+n\left(\frac{\omega_2-n\omega}{T_e}\right)\right] \times\left[f\left(\frac{\xi_{\mathbf{k}_\|}}{T}\right)-f\left(\frac{\omega_1+mv^2/2+\varepsilon^h_{\mathbf{k}_\|}+\mu}{T_e}\right)\right], \qquad (9)$$

$$\mathbf{r}_\omega = \frac{e\mathbf{E}_{\rm ac}}{m\omega^2}, \qquad (10)$$

in which $\omega = 2\pi f_{\rm ac}$ is the angular frequency, $\mathbf{q} = (\mathbf{q}_\|, q_z)$ is the three-dimensional phonon wave vector with $\mathbf{q}_\| = (q_x, q_y)$, $\omega_1 = k_x v$, $\omega_2 = \omega_1 + mv^2/2 + \varepsilon^h_{\mathbf{k}_\|} + \varepsilon_{s,\mathbf{k}_\|-\mathbf{q}_\|}$, $\xi_{\mathbf{k}_\|} = \varepsilon_{s,\mathbf{k}_\|} - \mu$, $\xi^h_{\mathbf{k}_\|} = \varepsilon^h_{\mathbf{k}_\|} - \mu^h$, $\varepsilon^h_{\mathbf{k}_\|} = E_g + \mathbf{k}_\|^2/(2m_h)$ is the hole dispersion with m_h the effective hole mass, and E_g is the band gap between the bottom of conduction band and the top of valence band. $\Pi_2(s',s,\mathbf{q}_\|,\Omega)$ is the imaginary part of electron-electron correlation functions, which shares the same expression with that given in reference [21]. $J_n(x)$ is the nth-order Bessel function, and $n(x) = 1/[\exp(x)-1]$ is the Bose function. The energy-gain rates of the electron system, $S_{\rm p}$ and $S_{\rm II}$, from the radiation field through the multiphoton process ($n = \pm1, \pm2, ...$) are respectively,

$$S_{\rm p} = \frac{1}{N}\sum_{s',s,\mathbf{q}_\|}\left|\widetilde{U}_{s's}(\mathbf{q}_\|)\right|^2 \times\sum_{n=-\infty}^{\infty} J_n^2(\mathbf{q}_\|\cdot\mathbf{r}_\omega)n\omega\Pi_2(s',s,\mathbf{q}_\|,\omega_0-n\omega) + \frac{2}{N}\sum_{s',s,\mathbf{q},\lambda}\left|\widetilde{M}_{s's}(\mathbf{q},\lambda)\right|^2 \times\sum_{n=-\infty}^{\infty} J_n^2(\mathbf{q}_\|\cdot\mathbf{r}_\omega)n\omega\Pi_2(s',s,\mathbf{q}_\|,\Omega_{\mathbf{q}\lambda}+\omega_0-n\omega) \times\left[\left(\frac{\Omega_{\mathbf{q}\lambda}}{T}\right)-n\left(\frac{\Omega_{\mathbf{q}\lambda}+\omega_0-n\omega}{T_e}\right)\right], \qquad (11)$$

and

$$S_{\rm II} = \frac{2}{N}\sum_{s',s,\mathbf{k}_\|,\mathbf{q}_\|}\left|\widetilde{M}^{\rm II}_{s',s}\left(\mathbf{q}_\|\right)\right|^2 \times\sum_{n=-\infty}^{\infty} J_n^2(\mathbf{q}_\|\cdot\mathbf{r}_\omega)n\omega\Pi_2(s',s,\mathbf{q}_\|,\omega_2-n\omega) \times\left[f\left(\frac{\xi_{\mathbf{k}_\|-\mathbf{q}_\|}}{T_e}\right)+n\left(\frac{\omega_2-n\omega}{T_e}\right)\right] \times\left[f\left(\frac{\xi_{\mathbf{k}_\|}}{T}\right)-f\left(\frac{\omega_1+mv^2/2+\varepsilon^h_k+\mu}{T_e}\right)\right], \qquad (12)$$

in which $\widetilde{U}_{s's}(\mathbf{q}_\|)$ and $\widetilde{M}_{s's}(\mathbf{q},\lambda)$ are the matrix elements of electron-impurity interaction and electron-phonon interaction, respectively. $\Omega_{\mathbf{q}\lambda}$ is the phonon frequency of wave vector $\mathbf{q}$ and the branch index λ. $\widetilde{M}^{\rm II}_{s',s}(\mathbf{q}_\|)$ is the Fourier representations of the band-band Coulomb interaction matrix element for II and Auger processes in 2D semiconductor system given by [21,22]

$$\widetilde{M}^{\rm II}_{s',s}\left(\mathbf{q}_\|\right) = I_{s',s}(q_\|)I_{cc}I_{cv}\frac{e^2}{2\epsilon\kappa\left(q_\|,0\right)q_\|} \equiv C_{\rm II}\frac{e^2}{2\epsilon\kappa\left(q_\|,0\right)q_\|}, \qquad (13)$$

where I_{cc} and I_{cv} are overlap integrals of conduction-conduction bands and conduction-valence bands, respectively. ϵ is the dielectric constant of semiconductor. $I_{s',s}(q_\|)$ is the form factor, and $\kappa\left(q_\|,0\right)$ is the screening factor (see Eq. (39) and (70–75) in Ref. [21]). $\kappa\left(q_\|,0\right)$ makes interband matrix element $\widetilde{M}^{\rm II}_{s',s}\left(\mathbf{q}_\|\right)$ be the short range, *i.e.*, it is finite at $q_\| = 0$. For the sake of simplicity, we set $C_{\rm II} \equiv I_{s',s}(q_\|)I_{cc}I_{cv}$ in equation (13) as the only adjustable parameter in the following calculations, which is determined by fitting to experiments.

3 Effect of an THz radiation on electron transport and II in InAs/AlSb HJ

Applying the above balance equations (2–4), we have performed a large number of numerical calculations of transport characteristics and II processes in InAs/AlSb HJ's, subjected to a small dc field and a THz electromagnetic radiation having various frequencies and amplitudes in the form of equation (1), $E(t) = E_0 + E_{\rm ac}\sin(2\pi f_{\rm ac}t)$. We consider the electron-acoustic-phonon scattering (*via* the deformation potential and the piezoelectric couplings), electron-polar-optical-phonon scattering (*via* the Fröhlich coupling), and elastic scattering both from the remote charged impurities and from the background impurities. Kane-type nonparabolic dispersion,

$$\varepsilon_s(\mathbf{k}_\|) = \varepsilon_s + \frac{1}{2\alpha}\left(\sqrt{1+\frac{2\alpha\mathbf{k}_\|{}^2}{m}}-1\right), \qquad (14)$$

Table 1. The material parameters for the InAs/AlSb HJ used in the calculations.

Parameter	Value	Unit	Ref.
Effective electron mass of InAs m	0.038	m_0	[5]
Effective hole mass of AlSb m_h	0.94	m_0	[23]
Band gap E_g	0.22	eV	[23]
Low-frequency dielectric constant κ	15.54	1	[24]
Optical dielectric κ_∞	11.74	1	[24]
Nonparabolicity of InAs α	2.73	eV^{-1}	[24]
Material density of InAs d	5.667	$\mathrm{g\,cm^{-3}}$	[25]
Longitudinal sound velocity v_{sl}	4.2×10^3	$\mathrm{m\,s^{-1}}$	[25]
Transverse sound velocity v_{st}	2.3×10^3	$\mathrm{m\,s^{-1}}$	[25]
Acoustic deformation potential E_1	5.8	eV	[26]
Piezoelectric constant e_{14}	4.26×10^8	V/m	[26]
Longitudinal optic phonon energy Ω_{LO}	29.5	meV	[26]

is assumed in calculating the inverse effective mass tensor $\mathcal{K}$ in equation (2), in which α is the nonparabolic factor. The role of the two lowest subbands ($s = 0, 1$) is taken into account. The energy separation between the bottoms of the zeroth and the first subbands, $\varepsilon_{10} = \varepsilon_1 - \varepsilon_0$, is taken to be 35 meV. We set the sheet density of InAs well $N_0 = 5 \times 10^{11}$ cm^{-2}, depletion layer charge density $N_{\mathrm{dep}} = 5 \times 10^{10}$ cm^{-2}, background impurity $n_I = 6.86 \times 10^{15}$ cm^{-3}, and remote impurities in AlSb barrier $N_I = 1.63 \times 10^{11}$ cm^{-2} located at a distance of $l = 10$ nm from the interface of the HJ. In the whole paper, the lattice temperature is set to be $T = 6$ K, and the small dc field is assumed to be $E_0 = 1.5$ V/m, same as that used in the experiments [5]. The very small dc component of the electric field E_0 almost doesn't play a role on the intense THz-induced transport and II process. One will get essentially identical electron temperature and the carrier density for $E_0 = 0$. The use of the small E_0 in the experiments [5] is just for getting a non-zero electron drift velocity and measuring the current in the circuit. The only adjustable parameter C_{II} appearing in equation (13) maintains unchanged $C_{\mathrm{II}} = 0.114$ in the calculations, which is determined by fitting to experiments. We have included contributions from as many optical channels as needed for reaching at a given integral accuracy of 10^{-4}, *i.e.*, the orders of the Bessel functions, n, in equations (9–12) are set to be large enough so that the integrals are convergent within the accuracy. The maximum of multiple photon channels has self-consistently been determined in the computing program. The larger the amplitude E_{ac} or the lower the frequency f_{ac} of the radiation field, the more optical channels have to be included for a given accuracy. The material parameters used here for InAs/AlSb HJ's are listed in Table 1.

When a small dc electric field E_0 and an intense THz field in the form of equation (1), $E(t) = E_0 + E_{\mathrm{ac}} \sin(2\pi f_{\mathrm{ac}} t)$, are applied to the direction parallel to the interface of InAs/AlSb HJ, the time evolution of electron velocity $v(t)$, electron temperature $T_e(t)$, and sheet density $N(t)$ have been monitored by directly solving equations (2–4). The II process is treated as a kind of scattering mechanism, and is included by accounting for the II-induced frictional acceleration A_{II}, II-induced energy loss-rate W_{II}, II-induced energy-gain rate S_{II} from the radiation field, and the electron-hole generation rate g. In Figures 1a–d we have respectively shown the calculated electron velocity $v(t)$, electron temperature $T_e(t)$, sheet density $N(t)$, and the net carrier generation rate $g(t)$ as functions of time for three radiation strengths $E_{\mathrm{ac}} = 35$, 38, and 40 kV/cm with the same frequency $f_{\mathrm{ac}} = 4$ THz. The corresponding locally-enlarged figures in the initial 60 ps are respectively plotted as the insets of Figures 1a–d. During the time evolution of the transport state two noticeable physical stages can be seen clearly, the quasi-steady state (QSS) and complete steady state (SS). As indicated by the insets of Figures 1a–d, after a rapid transient process of order of a few ps time delay from applying the THz electric field, the system arrives at a quasi-steady state, in which the carrier velocity, the electron temperature, and the electron-hole generation rate keep almost no change, while the total number of carriers increases with constant rate $g(= \mathrm{d}N/\mathrm{d}t)$ due to the II process with time evolution up to a time delay of order of 10^2 ps. The total number of carriers N in the QSS is apparently not too far from the initial carrier number N_0. QSS in the II process is important, since many experimental measurements of II-related transport, *e.g.*, the electron-hole generation rate, are taken during the QSS [5]. One may calculate the carrier velocity and the electron temperature of the QSS by setting the left-hand sides of equations (2, 3) to be zero ($\mathrm{d}\mathbf{v}/\mathrm{d}t = 0$ and $\mathrm{d}h_e/\mathrm{d}t = 0$). The carrier generation rate g is then obtained from equation (6). Since g is almost a constant within QSS, at a time delay τ_0 in QSS one has $\Delta N/N_0 \equiv (N - N_0)/N_0 = [N_0 \exp(g\tau_0) - N_0]/N_0 \approx g\tau_0$, thus $\Delta N/N_0$ is qualitatively comparable with g. In Figure 2a we have shown the calculated electron-hole generation rates g as a function of $1/E_{\mathrm{ac}}^2$ at two radiation frequencies $f_{\mathrm{ac}} = 0.42$ and 0.66 THz, respectively, at

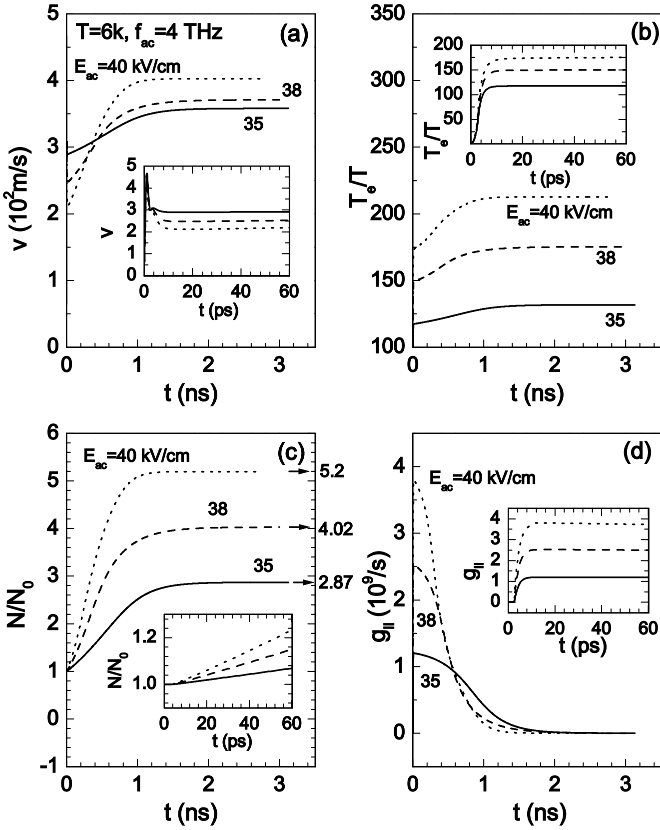

Fig. 1. (a) Calculated electron drift velocity $v(t)$, (b) electron temperature $T_e(t)$, (c) electron number $N(t)$, and (d) electron-hole generation rate $g(t)$ as functions of time in InAs/AlSb heterojunctions (HJ) driven by THz radiations having different for three THz radiation strengths $E_{ac} = 35$, 38, and 40 kV/cm with the same frequency $f_{ac} = 4$ THz at lattice temperature $T = 6$ K. The corresponding locally-enlarged figures in the initial 60 ps are respectively plotted as their insets.

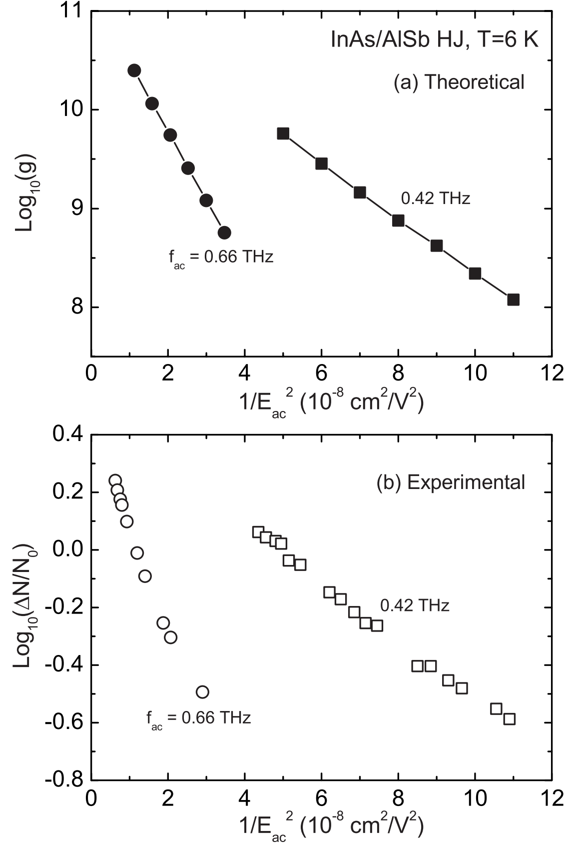

Fig. 2. (a) Calculated electron-hole generation rates g and (b) the experimental results of $\Delta N/N_0$ in InAs/AlSb HJ driven by THz radiations with two radiation frequencies $f_{ac} = 0.42$ and 0.66 THz, respectively, at $T = 6$ K.

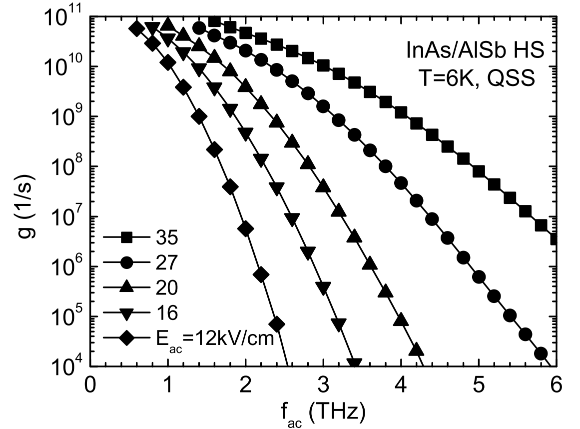

Fig. 3. Calculated electron-hole generation rate g *versus* the THz-radiation frequency f_{ac} in the quasi-steady-state (QSS) case at five different radiation strengths: $E_{ac} = 12$, 16, 20, 27, and 35 kV/cm, respectively, at $T = 6$ K.

$T = 6$ K. A qualitative agreement is observed between the calculated electron-hole generation rates g and the experimental results of $\Delta N/N_0$ (Fig. 2b) [5]. In order to have a deep insight into the dependence of the generation rates g on the radiation frequency f_{ac}, we have shown in Figure 3 the calculated g *versus* f_{ac} in the QSS case at five different radiation strengths: $E_{ac} = 12$, 16, 20, 27, and 35 kV/cm, respectively. It can be seen that, larger radiation strength and lower radiation frequency lead to a larger electron-hole generation rate g. It means that the role of THz radiation field on carrier transport and II process increases with increasing the factor $r_\omega = eE_{ac}/(m\omega^2)$.

In the following, we turn our attention to the complete steady-state case. We look back at Figures 1a–d, and find that, the QSS breaks up with the further evolution of time. The number of carriers increases more and more up to the complete SS with $N/N_0 = 2.87$, 4.02, and 5.2 respectively for $E_{ac} = 35$, 38, and 40 kV/cm (see Fig. 1c). The electron velocity and electron temperature also increase with the time evolution, and finally approach their SS at about $t > 2$ ns. At the complete SS case, electron-hole generation rate and recombination rate are equal, leading a zero net generation rate ($g = 0$) at all the radiation frequencies, as shown in Figure 1d. In the SS case, all the transport qualities become constants. To have a better insight into the SS case, we have performed much more SS calculations by setting the rights of equations (2–4) to be zero. In Figure 4a we have shown the carrier numbers N/N_0 in the SS case as a function of the radiation strength E_{ac}

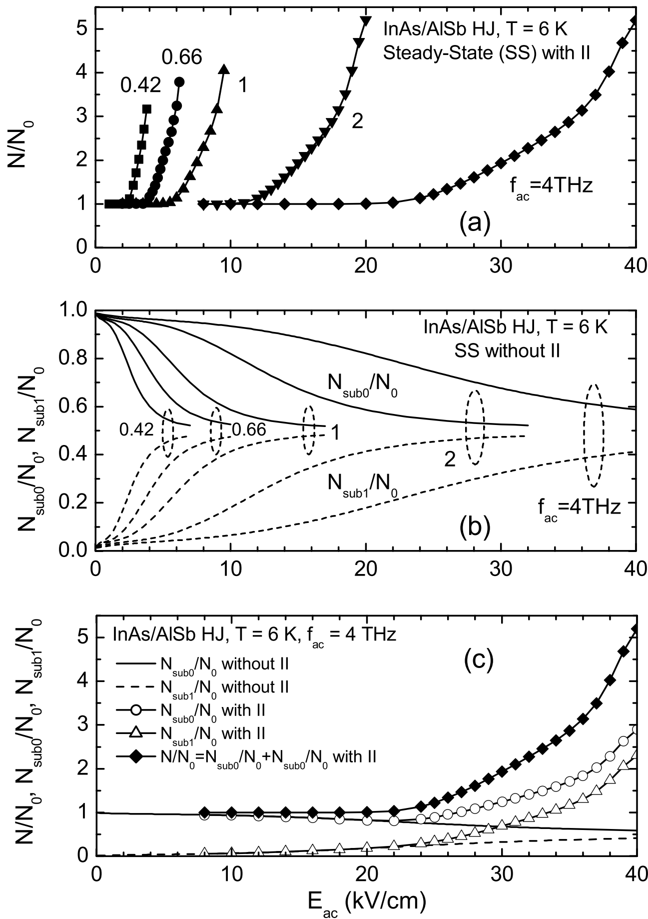

Fig. 4. (a) Steady-state carrier number N/N_0 as a function of the THz-radiation strength $E_{\rm ac}$ at $T = 6$ K and five different radiation frequencies $f_{ac} = 0.42$, 0.66, 1, 2, and 4 THz, respectively. (b) Fraction of the number of electrons accommodating the first and second subbands *versus* the THz-radiation strength without including the II process. The solid lines $N_{\rm sub0}/N_0$ are for the lowest subband $s = 0$, and the dashed lines $N_{\rm sub1}/N_0$ are for the second subband $s = 1$. (c) Comparison of electron accommodating numbers in the two subband with and without the II process at $T = 6$ K and $f_{\rm ac} = 4$ THz.

at five different radiation frequencies $f_{\rm ac} = 0.42$, 0.66, 1, 2, and 4 THz, respectively. For each frequency the carrier number increases with increasing $E_{\rm ac}$. For the lower frequency the carrier number increases quicker. For comparison, in Figures 4b and c we have shown the fraction of the number of electrons accommodating the first and second subbands *versus* the radiation fields with including and excluding the II process. In Figure 4b the solids lines, $N_{\rm sub0}/N_0$, are for the lowest subband $s = 0$, and the dashed lines, $N_{\rm sub1}/N_0$, are for the second subband $s = 1$, where $N \equiv N_{\rm sub0} + N_{\rm sub1} = N_0$ since we exclude the II process for Figure 4b. The electrons gain energy from the radiation field and gradually transfer into the second subband. The rates accommodating different subbands strongly depend on the driving frequency $f_{\rm ac}$. At the lower driving frequency $f_{\rm ac} = 0.42$ THz, the accommodation in the lowest subband decreases rapidly with increasing the radiation strength. In Figure 4c we have compared the electron numbers accommodating different subbands at $f_{\rm ac} = 4$ THz with and without II process. It's seen that after $E_{\rm ac} \approx 22$ kV/cm the II process begins to contribute the electron accommodations when compared to the case without II process. Finally, in Figure 5 we have shown the orders of the multiple-photon channels, $n_{b,\rm ei}$, $n_{b,\rm eph}$, and $n_{b,\rm II}$, respectively related to electron-impurity scattering, electron-phonon scattering, and II process at three radiation frequencies $f_{\rm ac} = 1$, 2, and 4 THz. They are self-consistently yielded by the computing program for reaching given accuracy of 10^{-4}. It's indicated that the order of II-related multiple-photon channels is usually larger than those related to electron-impurity scattering and electron-phonon scattering, and more multiple-photon channels are needed to be taken into account for larger radiation strength and lower radiation frequency.

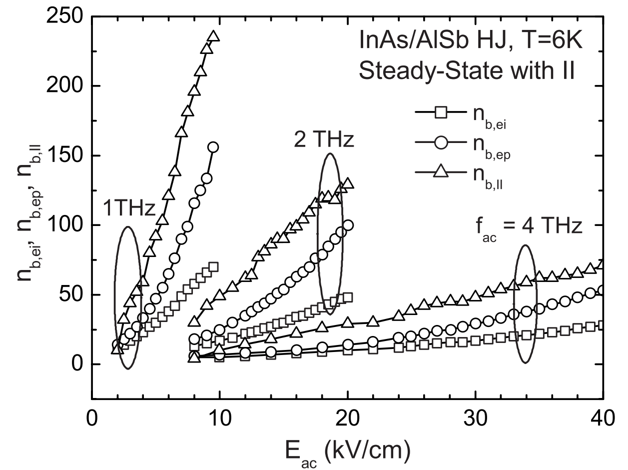

Fig. 5. The orders of the multiple-photon channels, $n_{b,\rm ei}$, $n_{b,\rm eph}$, and $n_{b,\rm II}$, respectively related to electron-impurity scattering, electron-phonon scattering, and II process in InAs/AlSb HJ at $T = 6$ K and $f_{\rm ac} = 1$, 2, and 4 THz, respectively. They are self-consistently yielded by the computing program.

4 Conclusions

In conclusion, we have extended the balance equations to include the impact ionization process induced by an intense THz radiation in two-dimensional semiconductor systems, and apply them to study the impact ionization effect on electron transport and electron-hole generation rate in InAs/AlSb HJ's induced by THz radiations having various frequency and strength. In the calculations, we considered the electron-acoustic-phonon scattering (*via* the deformation potential and the piezoelectric couplings), electron-polar-optical-phonon scattering (*via* the Fröhlich coupling), and elastic scattering both from the remote charged impurities and from the background impurities. As many as needed multiphoton channels are taken into account for yielding a given accuracy. By following the detailed time evolution we have been able to identify the

two different physical stages, the quasi-steady state and the complete steady state, of the THz-driven transport with the II process. Nonlinear transport characteristics, such as intersubband electron transfer rate and electron-hole generation rate, are calculated as functions of the THz radiation strength for various radiation frequencies. It is indicated that, the role of THz radiation field on carrier transport and II process increases with increasing the THz radiation strength or decreasing the THz radiation frequency. More multiple-photon channels are needed to be included for larger radiation strength and lower radiation frequency. Electron-hole generation rates are reasonably reproduced by the present calculations, and qualitatively compared to available experiments.

This work was supported by the Special Funds for Major State Basic Research Project (2001CCA02800 and G20000683), the National Natural Science Foundation of China (60136010, 60076011 and 90103017), and the Special Funds for Shanghai Optic Engineering (011661075).

References

1. N.G. Asmar, A.G. Markelz, E.G. Gwinn, J. Cerne, M.S. Sherwin, K.L. Campman, P.F. Hopkins, A.C. Gossard, Phys. Rev. B **51**, 18041 (1995)
2. B.J. Keay, S.J. Allen, Jr, J. Gala¡än, J.P. Kaminski, K.L. Camp-man, A.C. Gossard, U. Bhattacharya, M.J.W. Rodwell, Phys. Rev. Lett. **75**, 4098 (1995)
3. B.J. Keay, S. Zeuner, S.J. Allen, Jr, K.D. Maranowski, A.C. Gossard, U. Bhattacharya, M.J.W. Rodwell, Phys. Rev. Lett. **75**, 4102 (1995)
4. K. Unterrainer, B.J. Keay, M.C. Wanke, S.J. Allen, D. Leonard, G. Medeiros-Ribeiro, U. Bhattacharya, M.J.W. Rodwell, Phys. Rev. Lett. **76**, 2973 (1996)
5. A.G. Markelz, N.G. Asmar, B. Brar, E.G. Gwinn, Appl. Phys. Lett. **69**, 3975 (1996)
6. X.L. Lei, J. Appl. Phys. **84**, 1396 (1998)
7. X.L. Lei, J. Phys. Cond. Matt. **10**, 3201 (1998)
8. X.L. Lei, H.L. Cui, Eur. Phys. J. B **4**, 513 (1998)
9. J.C. Cao, H.C. Liu, X.L. Lei, J. Appl. Phys. **87**, 2867 (2000)
10. J.C. Cao, H.C. Liu, X.L. Lei, A.G.U. Perera, Phys. Rev. B **63**, 115308 (2001)
11. J.C. Cao, X.L. Lei, A.Z. Li, H.C. Liu, Appl. Phys. Lett. **78**, 2524 (2001)
12. J.C. Cao, A.Z. Li, X.L. Lei, S.L. Feng, Appl. Phys. Lett. **79**, 3524 (2001)
13. X.L. Lei, C.S. Ting, Phys. Rev. B **32**, 1112 (1985)
14. X.L. Lei, N.J.M. Horing, H.C. Cui, Phys. Rev. Lett. **66**, 3277 (1991)
15. H. Xie, W.I. Wang, J.R. Meyer, J. Appl. Phys. **76**, 92 (1994)
16. C.R. Bolognesi, E.J. Caine, H. Kroemer, IEEE Electron Device Lett. **15**, 16 (1994)
17. A.G. Markelz, N.G. Gwinn, M.S. Sherwin, C. Nguyen, H. Kroemer, Solid State Electron. **37**, 1243 (1994)
18. E. Dupont, H.C. Liu, R.Q. Yang, J. Appl. Phys. **86**, 7195 (1999)
19. X.F. Wang, X.L. Lei, J. Phys. Cond. Matt. **7**, 7871 (1995)
20. J.C. Cao, X.L. Lei, Solid-State Electron. **42**, 419 (1998); Euro. Phys. J. B **7**, 79 (1999)
21. X.L. Lei, J.L. Birman, C.S. Ting, J. Appl. Phys. **58**, 2270 (1985)
22. T. Ando, A.B. Fowler, F. Stern, Rev. Mod. Phys. **54**, 437 (1982)
23. B. Brar, H. Kroemer, J. Appl. Phys. **83**, 894 (1998)
24. B.R. Nag, *Electron Transport in Compound Semiconductors* (Springer-Verlag, Berlin, 1980)
25. L. Reggiani, *Hot-electron Transport in Semiconductors* (Springer-Verlag, Berlin, 1985)
26. K.W. Böer, *Survey of semiconductor physics: electrons and other particles in bulk semiconductors* (New York: Van Nostrand Reinhold, 1990)